

Research Article

Geometric Modeling of *Rosa roxburghii* Fruit Based on Three-Dimensional Point Cloud Reconstruction

Zhiping Xie , Yancheng Lang , and Luqi Chen

School of Mechanical & Electrical Engineering, Guizhou Normal University, Guizhou, Guiyang 550025, China

Correspondence should be addressed to Zhiping Xie; xzpfeinia@163.com

Received 31 March 2021; Accepted 20 September 2021; Published 29 September 2021

Academic Editor: Nesibe E. Kafkas

Copyright © 2021 Zhiping Xie et al. This is an open access article distributed under the Creative Commons Attribution License, which permits unrestricted use, distribution, and reproduction in any medium, provided the original work is properly cited.

Fruit three-dimensional (3D) model is crucial to estimating its geometrical and mechanical properties and improving the level of fruit mechanical processing. Considering the complex geometrical features and the required model accuracy, this paper proposed a 3D point cloud reconstruction method for the *Rosa roxburghii* fruit based on a three-dimensional laser scanner, including 3D point cloud generation, point cloud registration, fruit thorns segmentation, and 3D reconstruction. The 3D laser scanner was used to obtain the original 3D point cloud data of the *Rosa roxburghii* fruit, and then the fruit thorns data were removed by the segmentation algorithm combining the statistical outlier removal and radius outlier removal. By analyzing the effects of five-point cloud simplification methods, the optimal simplification method was determined. The Poisson reconstruction algorithm, the screened Poisson reconstruction algorithm, the greedy projection triangulation algorithm, and the Delaunay triangulation algorithm were utilized to reconstruct the fruit model. The number of model vertices, the number of facets, and the relative volume error were used to determine the best reconstruction algorithm. The results indicated that this model can better reconstruct the actual surface of *Rosa roxburghii* fruit. The method provides a reference for the related application.

1. Introduction

Rosa roxburghii is a perennial deciduous shrub of the Rosaceae *Rosa* genus, which is mainly distributed in southwest areas in China, such as Yunnan, Guizhou, and Sichuan [1, 2]. *Rosa roxburghii* fruit has high nutritional value and health function [2–4], and it is a kind of fruit with great economic value. In recent years, the *Rosa roxburghii* has been vigorously promoted in Guizhou, which has 133,000 hectares of planting area and 100,000 tons of annual output of fresh fruits. However, the degree of automation in the fruit processing process is not high, especially the process of fruit picking and fruit pedicle removal. In order to realize the whole automation of fruit processing, it is particularly important for the three-dimensional digital reconstruction of *Rosa roxburghii* fruit.

3D reconstruction of agricultural and forestry crops has become an important research method in agricultural scientific research. In this method, plants with complex shapes can be studied by combining agricultural production

knowledge and computer graphics technology [5, 6]. The 3D reconstruction methods of agricultural and forestry crops mainly include the image-based reconstruction, the parametric model-based reconstruction, and the 3D point cloud-based reconstruction [7–10].

The image-based reconstruction method is to use multiple images to reconstruct the surface model of crops. Quan et al. [11] and Wang et al. [12] reconstructed 3D models of plants and corn ears, respectively, based on image technology. A robotic arm with a camera was used to collect a series of two-dimensional images of the object to achieve three-dimensional reconstruction, and the influence of the motion of the robotic arm on the accuracy of the three-dimensional image reconstruction was studied [13]. This method has the advantage of quickness and simplicity but has the defect in detailed features.

The parametric model-based reconstruction method needs to collect the surface characteristic parameters of the object. Kempthorne et al. [14] applied the discrete smoothing D^2 -spline algorithms to reconstruct the leaf

surfaces from point cloud data. Hu et al. [15] presented the method based on 3D visualization to measure the leaf area, length, and width of poplar seedlings. Tinoco et al. [16] modeled the topological structure of coffee fruits based on Bezier curves and performed finite element analysis. The accuracy of this method is not very high, and it is not suitable for the reconstruction of complex shapes.

The 3D point cloud-based reconstruction method relies on the instrument to directly obtain the 3D information of the measured object, which has high accuracy and wide applications. Sun and Wang [17] proposed the 3D rapid greenhouse plant point cloud reconstruction method based on autonomous Kinect v2 sensor position calibration. Xie et al. [18] used the terrestrial LiDAR to obtain point cloud data of a single tree and reconstructed the 3D model of the tree with leaves. Zermas et al. [19] utilized an unmanned aerial vehicle and the handheld camera with structure from motion to reconstruct 3D canopies of small groups of corn plants. An accurate 3D point cloud data is critical for these methods, but the methods of using the Kinect v2 sensor, terrestrial LiDAR, and unmanned aerial vehicle to obtain point cloud data ignore or simplify the object details. In addition, the prickly surface of *Rosa roxburghii* fruit brings challenges to the acquisition of the 3D point cloud of the fruit.

The 3D laser scanner is widely used to obtain 3D point cloud data due to the advantages of noncontact and high accuracy [20]. Zhang et al. [21] employed the 3D laser scanning technology to obtain the point cloud data of apple tree leaves and achieved 3D reconstruction of apple tree leaves. Considering that the detailed features of the fruit surface can be acquired by a 3D laser scanner, it is a novel idea to use the 3D laser scanner to obtain the point cloud data of the *Rosa roxburghii* fruit.

The novelties and contributions of this paper are summarized as follows:

- (1) Proposing a 3D point cloud reconstruction method for the *Rosa roxburghii* fruit based on the 3D laser scanner
- (2) Designing a fruit thorns segmentation algorithm combining statistical outlier removal and radius outlier removal and improving the accuracy of the 3D model of *Rosa roxburghii* fruit
- (3) Proposing a volume calculation method for *Rosa roxburghii* fruit based on cylindrical coordinates to verify the accuracy of the reconstructed model

The main purpose of this paper is to obtain an accurate 3D geometric model of the *Rosa roxburghii* fruit without thorns which will facilitate the subsequent finite element simulation of the mechanical properties and the design of related mechanical processing equipment. The rest of this paper is arranged as follows: in Section 2, the measurement system, point cloud registration, segmentation algorithm, and 3D reconstruction algorithm are described in detail. In Section 3, the results of point cloud segmentation, simplification, and reconstruction are discussed in detail, and the 3D reconstruction method is verified. Section 4 summarizes this paper.

2. Materials and Methods

2.1. Structure and Principle of the Measurement System. The schematic diagram of obtaining point cloud data of *Rosa roxburghii* fruit is shown in Figure 1. Figure 1 shows that *Rosa roxburghii* fruit has sharp thorns and an uneven surface. The noncontact 3D laser scanner (Laser-RE600111) was used to obtain the surface of *Rosa roxburghii* in this experiment. And its collection frequency, scanning accuracy, scanning distance, and measurement range are 1000–15000/s, 0.02 mm, 150 mm, and 600 mm (length) × 500 mm (width) × 400 mm (height), respectively. The operation process of collecting data was divided into 3 steps. Firstly, a white developer was sprayed on the fruit surface to obtain a good diffuse reflection shape, and then the laser scanner was employed to measure the horizontal and vertical point cloud data of the fruit in the rotating state. Secondly, the point cloud data from different angles were manually registered through three preset marker points, and then the point cloud processing software (Geomagic studio 2017) was used for secondary fine registration. Finally, the final point cloud format was saved as a PCD file to facilitate the subsequent running of algorithms. The point cloud data collection experiment of *Rosa roxburghii* was completed in the reverse engineering laboratory.

In the paper, the point cloud images were all visualized by MATLAB R2018b. The 3D reconstruction flowchart of *Rosa roxburghii* fruit is shown in Figure 2.

2.2. Registration of the Point Cloud of Fruit. Since the pedicle end of the fruit is concave and the stalk end is approximately flat, the point cloud data of the top and bottom of the fruit cannot be obtained for the vertical position. Therefore, it is necessary to rotate the fruit to obtain the top and bottom point cloud data. In the experiment, the fruit was placed vertically along the z -axis (Figure 1), and the platform was rotated 360° to collect point cloud data around the fruit. In order to make the point cloud on the top and bottom of the fruit and the point cloud on the side of the fruit in the same coordinate system, the fruit must be rotated 90° and −90° (rotate counterclockwise as positive direction) around the y -axis (Figure 1), respectively. Through the rotation matrix (equation (1)), the point cloud data on the top and bottom of the fruit and the point cloud data on the side of the fruit can be unified into the same coordinate system by iterative closest point (ICP) [22] algorithm. The registration process of fruit point cloud data is shown in Figure 3. The relationship between point cloud data before and after rotation is shown in equation (2):

$$R_y(\alpha) = \begin{pmatrix} \cos \alpha & 0 & \sin \alpha \\ 0 & 1 & 0 \\ -\sin \alpha & 0 & \cos \alpha \end{pmatrix}, \quad (1)$$

$$\text{pointcloud}'_m(x_n, y_n, z_n) = \text{pointcloud}_m(x_n, y_n, z_n) \times R_y(\alpha), \quad (2)$$

where pointcloud_m is the m th point cloud data before rotation adjustment; (x_n, y_n, z_n) are the coordinates of the point

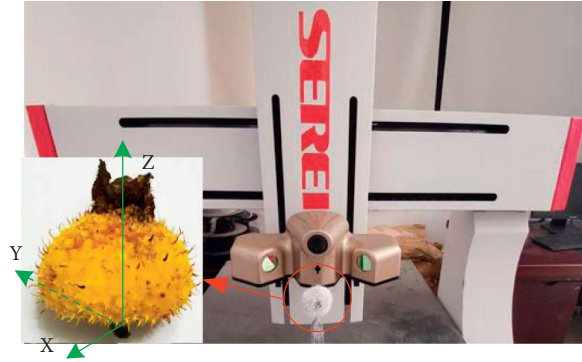


FIGURE 1: Schematic diagram of point cloud data acquisition.

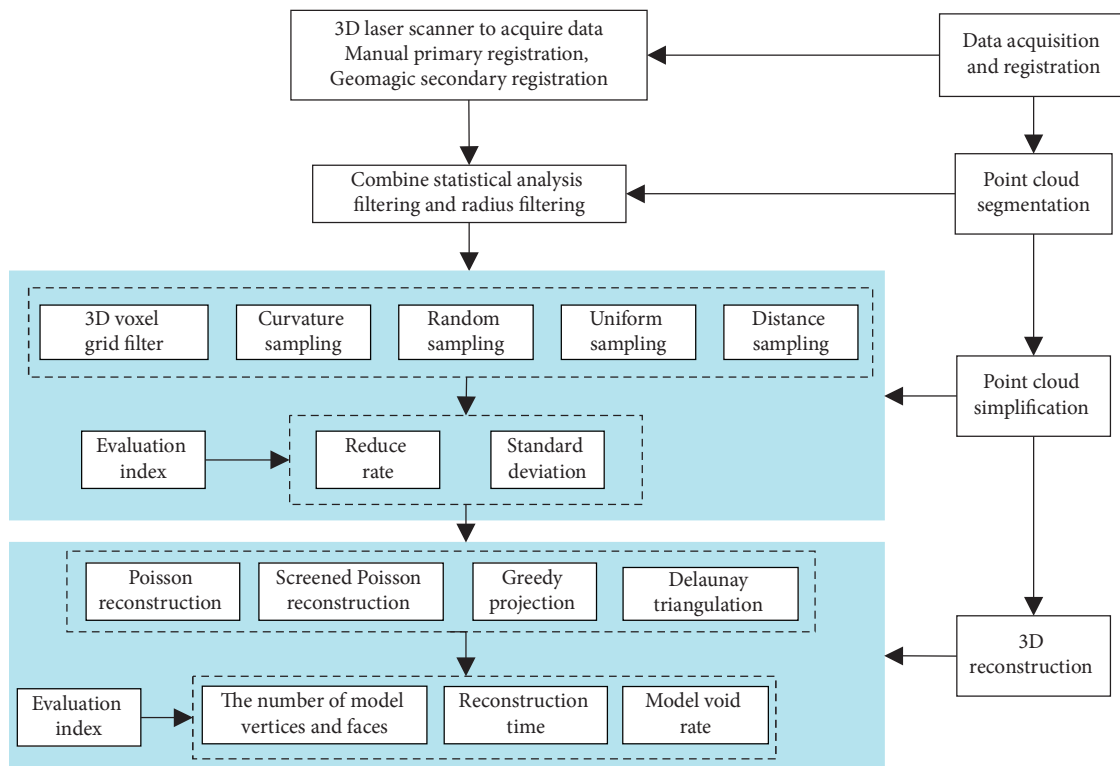
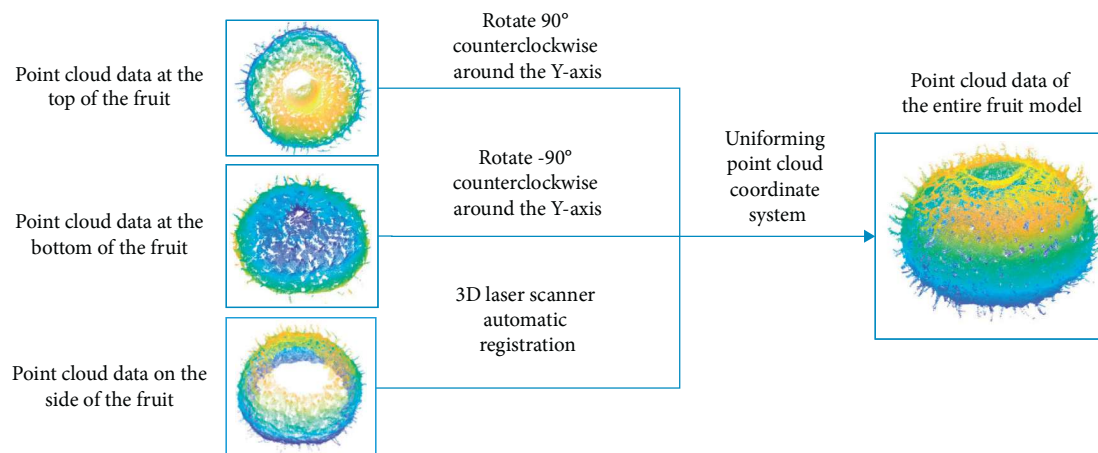
FIGURE 2: Flowchart of 3D reconstruction of *Rosa roxburghii* fruit.

FIGURE 3: Registering the entire model of fruit through point cloud data from different coordinate systems.

cloud; n is the number of point clouds; $\text{pointcloud}'_m$ is the m th point cloud data after rotation adjustment; $R_y(\alpha)$ is rotation matrix of the fruit rotating around the y -axis; and α is the rotation angle of the point cloud.

In Figure 3, the point cloud data of the side, top, and bottom of the *Rosa roxburghii* fruit were scanned by a platform that can rotate at a uniform speed, and they were registered together through the corresponding rotation matrix. After the point cloud registration process, the complete point cloud of *Rosa roxburghii* fruit was obtained for fruit thorns segmentation and point cloud simplification.

2.3. Segmentation Algorithm of Fruit Thorns. Generally, it is inevitable to be affected by the accuracy of the instrument, the operation of personnel, and external environmental factors, so that the collected point cloud data contains noise, which have adverse effects on the subsequent operation and 3D reconstruction of the point cloud data [23]. Besides, the analysis of mechanical properties of *Rosa roxburghii* fruit is affected by the fruit thorns on the fruit surface, which need to be removed when building the geometric model. The segmentation algorithm combining the statistical outlier removal [24, 25] and radius outlier removal [26] was proposed to remove noise and fruit thorns. A flowchart of a fruit thorn segmentation algorithm was proposed, as shown in Figure 4. The steps of the segmentation algorithm can be summarized as follows:

Step 1: the point cloud dataset is assumed to be $P = \{p_1, p_2, \dots, p_n\}$, and the three-dimensional space coordinates of any point p_i is (x_i, y_i, z_i) . The size k value of the neighborhood is input, and then the 3D space coordinates of the k neighbors of p_i are expressed as (x_j, y_j, z_j) . The formula for calculating the average distance d_i from each point to its k neighbors is as follows:

$$d_i = \frac{1}{k} \sum_{j=1}^k \sqrt{(x_i - x_j)^2 + (y_i - y_j)^2 + (z_i - z_j)^2}. \quad (3)$$

Step 2: the mean μ and standard deviation σ of the average distance between each point's neighborhoods are calculated. Their calculation formulas are as follows:

$$\mu = \sum_{i=1}^n \frac{d_i}{n}, \quad (4)$$

$$\sigma = \sqrt{\frac{1}{n} \sum_{i=1}^n (d_i - \mu)^2}, \quad (5)$$

where n is the original point cloud number of *Rosa roxburghii* fruit.

Step 3: each point of the dataset is judged on whether it is an outlier. The standard deviation multiple α is set as a constant; if $d > \mu + \alpha\sigma$, the point is judged as an outlier, and it is deleted; and if $d < \mu - \alpha\sigma$, the point is judged to be a normal point, and it is retained.

Step 4: steps 1–3 are repeated until all points are calculated and judged.

Step 5: the remaining outliers are removed by radius outlier removal. The threshold N of the number of k nearest neighbors and the radius r of the search sphere are, respectively, determined. If the number of neighbors of a point within the radius r of the sphere is less than the threshold N , the point is determined to be an outlier and can be deleted. Otherwise, the point is a normal point and retained.

Step 6: until all the points are traversed, the segmentation algorithm is ended.

2.4. Point Cloud 3D Reconstruction. Nowadays, some well-known reconstruction algorithms based on point cloud have been proven to have good reconstruction effects on solid surfaces, such as ball pivoting [27], Poisson reconstruction [28], screened Poisson reconstruction [29], marching cubes [30], alpha shapes [31], greedy projection triangulation [32], and Delaunay triangulation [33]. This paper uses the Poisson reconstruction algorithm, screened Poisson reconstruction algorithm, greedy projection triangulation algorithm, and Delaunay triangulation algorithm to reconstruct the 3D model of *Rosa roxburghii* fruit.

2.4.1. Poisson Reconstruction Algorithm. The Poisson reconstruction algorithm belongs to the implicit function of the triangle mesh reconstruction algorithm, in which the advantages of local fitting and global fitting are taken into account [34]. While the global smoothness of the reconstructed surface is realized, the local detailed features are preserved, and the reconstruction effect for closed surfaces is better. Except for the point samples around the surface, the gradient of the indicator function everywhere is a vector field with a value of zero. Therefore, the indicator function is equal to the inner normal of the surface. The core idea of the algorithm is as follows: for an unknown 3D entity M , to solve an indicator function χ after its surface ∂M is smoothed, so that its gradient field is equal to the divergence of the surface ∂M vector field \vec{V} [28]:

$$\begin{aligned} \Delta\chi &= \nabla \cdot \vec{V}, \\ \nabla(\chi_M * \tilde{F})(q_o) &= \int_{\partial M} \tilde{F}_P(q_o) \vec{N}_{\partial M}(p) dp \\ &\approx \sum_{s \in S} |p_s| \tilde{F}_{s,p}(q) s \cdot \vec{N}, \end{aligned} \quad (6)$$

where χ_M is the indicator function of M , \tilde{F} shows the smoothing filter function, \vec{N} denotes the inward normal of the point, and p_s is the area of the small patch.

The approximate steps of the Poisson reconstruction algorithm are as follows [35]: (1) discretization function space through Octree, (2) estimating the vector field by using principal component analysis, (3) solving the Poisson equation, and (4) extracting the isosurface. The flowchart of the algorithm is shown in Figure 5.

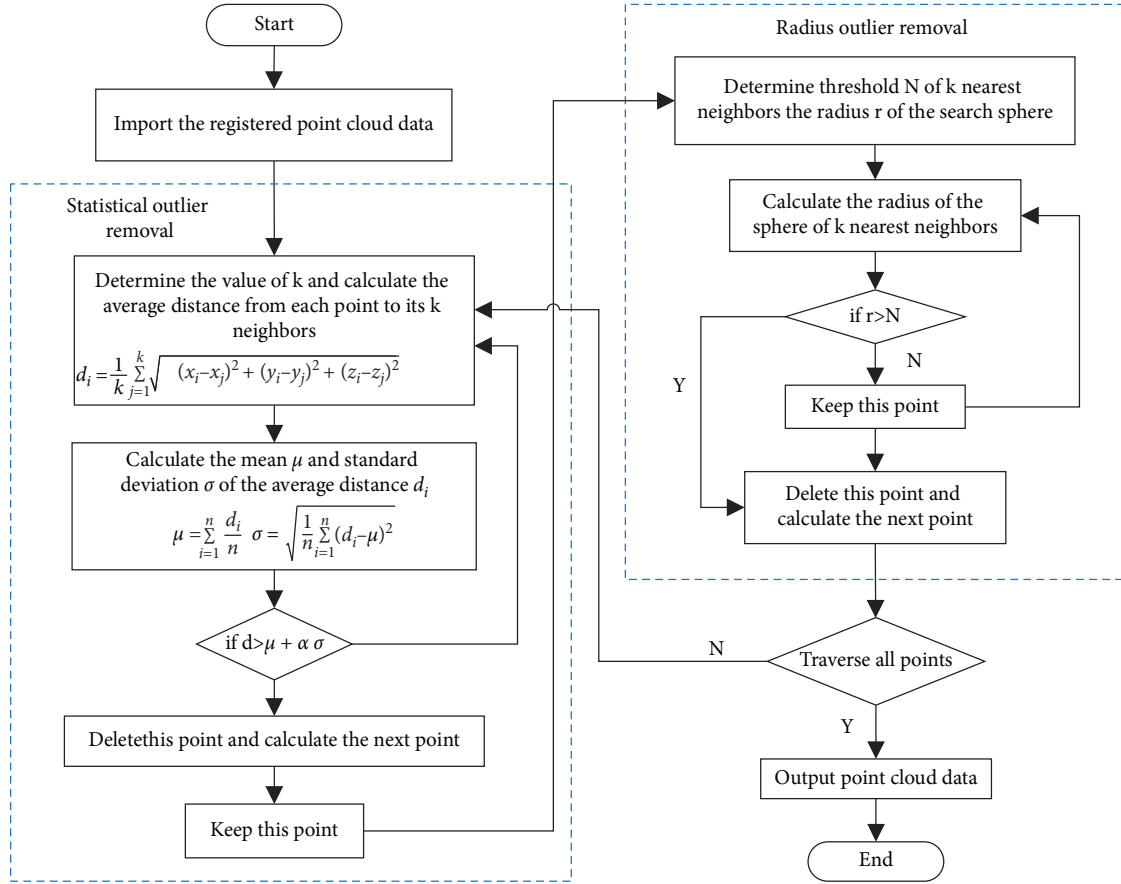


FIGURE 4: Flowchart of the segmentation algorithm of fruit thorns.

2.4.2. Screened Poisson Reconstruction Algorithm.

Although in the process of solving Poisson's equation, an approximate solution of the indicator function can be obtained, this approximate solution may be very different from the real indicator function. In order to avoid this shortcoming, Kazhdan and Hoppe [29] proposed the screened Poisson surface reconstruction algorithm, which introduces the constraints of the point set to turn the problem solving into the process of solving the screened Poisson equation to make the solved indicator function more accurate. Figure 6 shows the flowchart of the screened Poisson reconstruction algorithm. The detailed steps of the screened Poisson reconstruction algorithm are as follows: (1) incorporating point constraints, (2) scale-independent screening, (3) discretizing the function space with an Octree, (4) estimating the vector field, and (5) solving the screened Poisson equation as follows:

$$(\Delta - \alpha \vec{I})\chi = \nabla \cdot \vec{V}. \quad (7)$$

2.4.3. Greedy Projection Triangulation Algorithm. The greedy projection triangulation algorithm is a surface reconstruction technology based on triangulation and the greedy algorithm. The idea of the greedy algorithm is to simplify complex problems without considering the overall situation, but only seeking local optimal solutions. And the

greedy algorithm follows three criteria, namely, the nearest greedy criterion, the nearest neighbor greedy criterion, and the directed greedy criterion. The basic steps of the algorithm are as follows [32]:

Step 1: at a certain point, the local tangent plane perpendicular to the normal vector of the point should be determined first.

Step 2: in the three-dimensional point cloud set, an initial triangle is determined, and the k nearest neighbors of the three points constituting the triangle are searched. These three points and their k neighboring points are projected on the tangent plane of the point along the normal direction.

Step 3: the two-dimensional triangulation of the projection point on the projection plane is performed.

Step 4: the optimal expansion point on the two-dimensional plane is mapped back to the three-dimensional space to form a spatial triangle grid.

Step 5: steps 1–4 are looped until a complete mesh surface is formed, and then the algorithm is stopped.

2.4.4. Delaunay Triangulation Algorithm. Delaunay triangulation is a classic triangle mesh reconstruction algorithm, which determines the scattered point cloud space topology

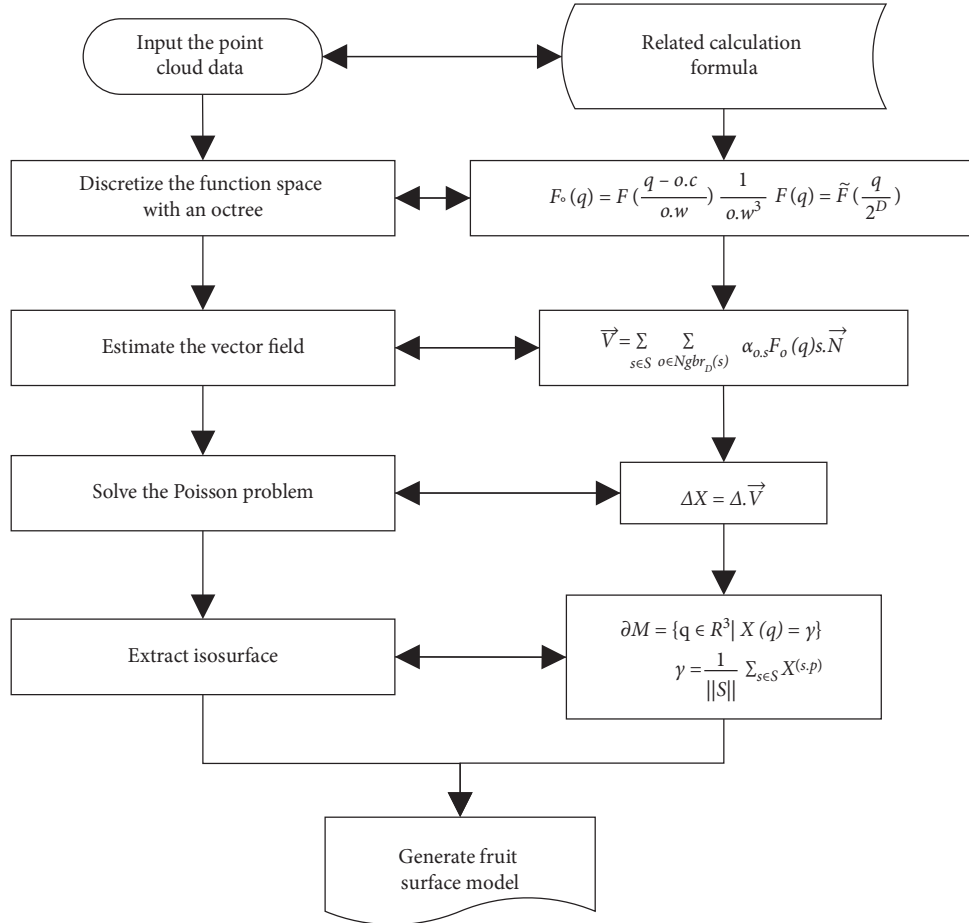


FIGURE 5: Flowchart of the Poisson reconstruction algorithm.

by constructing a triangle mesh. In the triangulation algorithm, the Delaunay triangulation algorithm can obtain the optimal triangulation grid. According to the different implementation processes, Delaunay triangulation can be divided into point-by-point insertion method [36], region growth method, divide-and-conquer method [37], and random Delaunay filtering method [38]. In this paper, the Delaunay triangulation algorithm based on region growth is adopted. The basic steps of the algorithm are as follows [33]:

Step 1: any point in the point set is selected, and the nearest neighbor point to that point is found.

Step 2: the line connecting these two points is used as the initial edge to expand outward, and the third point that can form the best Delaunay triangle with the initial edge is searched.

Step 3: the initial side and the third point form a new triangle, and the other two sides of the new triangle except for the initial side are added to the edge queue, but the existing sides cannot be added repeatedly.

Step 4: steps 1–3 are repeated until the surface growth is completed.

3. Results and Discussion

3.1. Result of Point Cloud Segmentation. The original 3D point cloud of the *Rosa roxburghii* obtained by the 3D laser scanner is shown in Figure 7(a), and the total number of point clouds contained 230674 points. The 3D point cloud after segmentation using the statistical outlier removal algorithm [24, 25] is shown in Figure 7(b), and the number of neighbor points k and the standard deviation multiple were set to 35 and 1.3, respectively. The 3D point cloud after segmentation using the radius outlier removal algorithm [26] is shown in Figure 7(c), and the threshold N of the number of neighbor points and the radius r of the sphere were taken as 60 and 0.8, respectively. The 3D point cloud after segmentation using the bilateral filtering algorithm [39] is shown in Figure 7(d). It can effectively remove the noise points, but it cannot effectively remove the thorns. The 3D point cloud after segmentation using the proposed separation algorithm is shown in Figure 7(e), and the number of point cloud data after segmentation retains 206031 points. It can be seen from Figure 7(e) that the thorns and noise points on the surface of *Rosa roxburghii* fruit were basically

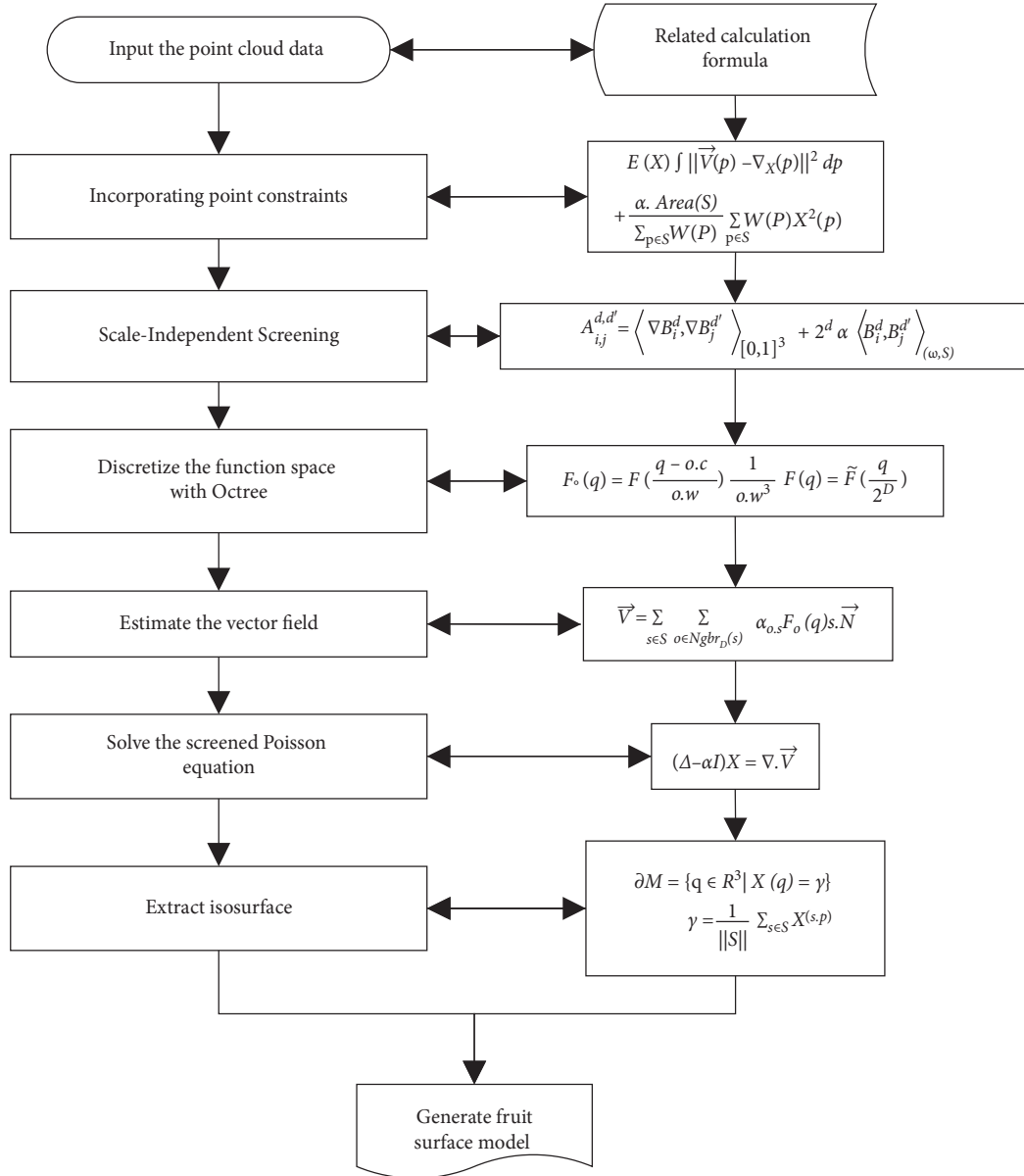


FIGURE 6: Flowchart of the screened Poisson reconstruction algorithm.

removed, indicating that the segmentation effect was particularly obvious. Figures 7(a)–7(e) show that the four segmentation algorithms can effectively remove noise, and the proposed segmentation algorithm can remove fruit thorns better than the other three segmentation algorithms.

3.2. Comparison of Different Simplification Methods. Owing to the high accuracy of the 3D laser scanner, the amount of point cloud data collected is greatly large, which not only contains the geometric information of the *Rosa roxburghii* fruit but also has redundant data points that need to be eliminated [40]. Plenty of time is consumed, and a large amount of computer memory is occupied in the data processing process. Furthermore, all points need not be calculated at the stage of 3D reconstruction, as long as the feature points are retained. In order to balance the

contradiction between time and efficiency, it is necessary to streamline the point cloud data for the grid reconstruction process [41]. The 3D voxel grid filter method [42, 43], the curvature sampling method [44], the random sampling method, the uniform sampling method, and the distance sampling method are common simplification methods.

In the point cloud streamlining processing stage, the 3D voxel grid filter method, the curvature sampling method, the random sampling method, the uniform sampling method, and the distance sampling method were compared and analyzed, and the best sampling method was determined as the simplification algorithm. In order to assess the point cloud simplification effect of different sampling methods, the simplification rate η and average error ε were introduced to evaluate the simplification effect. The simplification rate η was defined as follows:

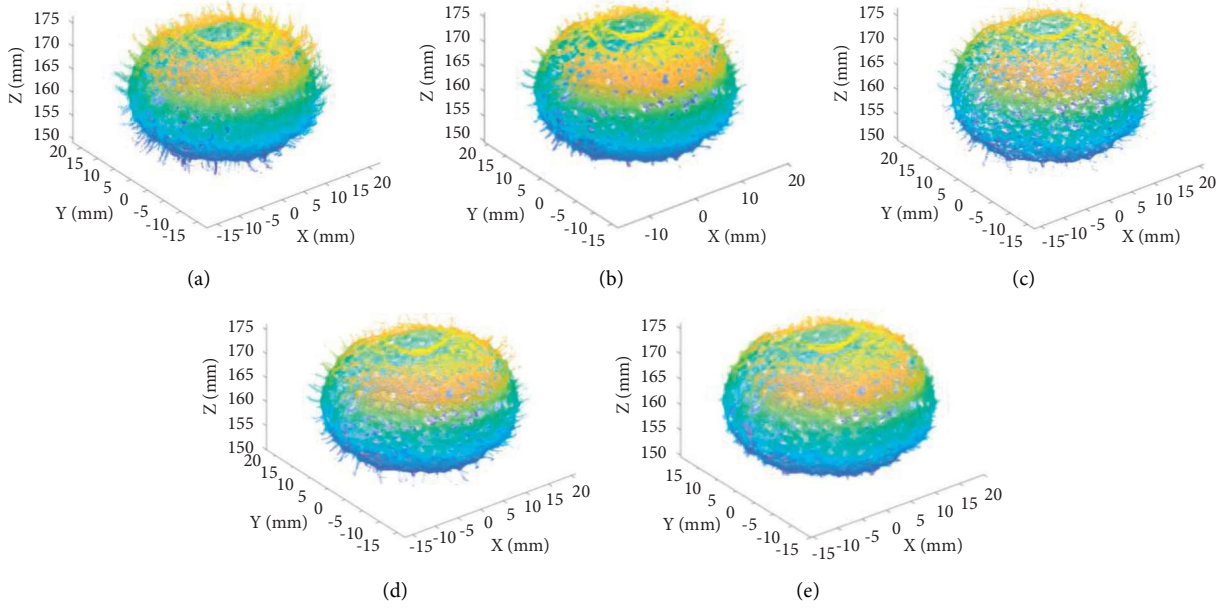


FIGURE 7: Original 3D point cloud and result of point cloud segmentation. (a) Original point cloud; (b) statistical outlier removal; (c) radius outlier removal; (d) bilateral filtering; (e) proposed algorithm.

$$\eta = \frac{n_1 - n_2}{n_1} \times 100\%, \quad (8)$$

where n_1 represents the number of point clouds before simplification and n_2 represents the number of point clouds before simplification.

The average error ε is defined as follows [45]:

$$\varepsilon = \frac{1}{\|S\|} \sum_{u \in S} d(u, v), \quad (9)$$

where $d(u, v)$ represents the Euclidean distance between the sampling point u of the original surface S of the fruit and the projection point v of the simplified surface.

Generally, when the simplification rate is constant, the greater the average error is, the greater the deviation between the surface and the sampled data is and vice versa. Table 1 shows the simplification rate and average error of the point cloud reconstruction model with different sampling methods. The effect of different sampling methods on the point cloud is shown in Figure 8. It can be seen from Table 1 that when simplification rate η was approximately 90%, the average error of the 3D voxel grid filter method is the smallest in the five sampling methods, and the average error of the random sampling method is the largest. Moreover, it can be seen from Figure 8 that the random sampling method did not consider the detailed feature points to randomly sample and streamline, which resulted in uneven point cloud sampling. From the effect point of view, although the uniform sampling method and the distance sampling method were more uniform, the detail feature of the point cloud was not obvious. Although the curvature sampling method can retain feature points well, the standard deviation of the reconstructed model is higher than that of the 3D voxel grid filter method. Considering the average error of the

reconstruction model and the advantages and disadvantages of the point cloud sampling methods, the 3D voxel grid filter can retain the features better and the error was small, so this method was selected to simplify the point cloud of the *Rosa roxburghii* fruit.

3.3. Comparison of Different Reconstruction Algorithms.

The above four reconstruction algorithms were used in the 3D reconstruction of *Rosa roxburghii* fruit for experimental comparison, and the effect of the fruit reconstruction model is shown in Figure 9. Based on the number of vertices (NMV), the number of facets (NMF), and the relative volume error (RVE) of the fruit reconstruction model, the reconstruction accuracies of the four reconstruction algorithm models were analyzed, which are shown in Table 2. The three evaluation indicators selected in this article are described in detail as follows.

3.3.1. Number of Model Vertices (NMV). For the triangular mesh reconstruction algorithm, the reconstructed mesh model is composed of a large number of triangular facets, and the number of vertices of the triangular facets represents the degree of fineness of the facets. The finer the patch, the higher the realism of the model.

3.3.2. Number of Model Facets (NMF). The larger the number of triangles is, the more obvious the details of the reconstructed model are, and the higher the accuracy of the model is.

3.3.3. Relative Volume Error (RVE). The actual volume of the *Rosa roxburghii* fruit is 14.2 cm^3 by calculating the volume of water discharged from the container, and the

TABLE 1: Average errors of different point cloud simplification methods.

Simplification methods	Points after segmentation	Points after simplifying	Simplification rate η	Average error ε (mm)
3D voxel grid filter	206031	20978	89.82	0.1941
Curvature sampling	206031	21013	89.80	0.2233
Random sampling	206031	20603	90.00	0.2317
Uniform sampling	206031	20643	89.98	0.2205
Distance sampling	206031	20311	90.14	0.2278

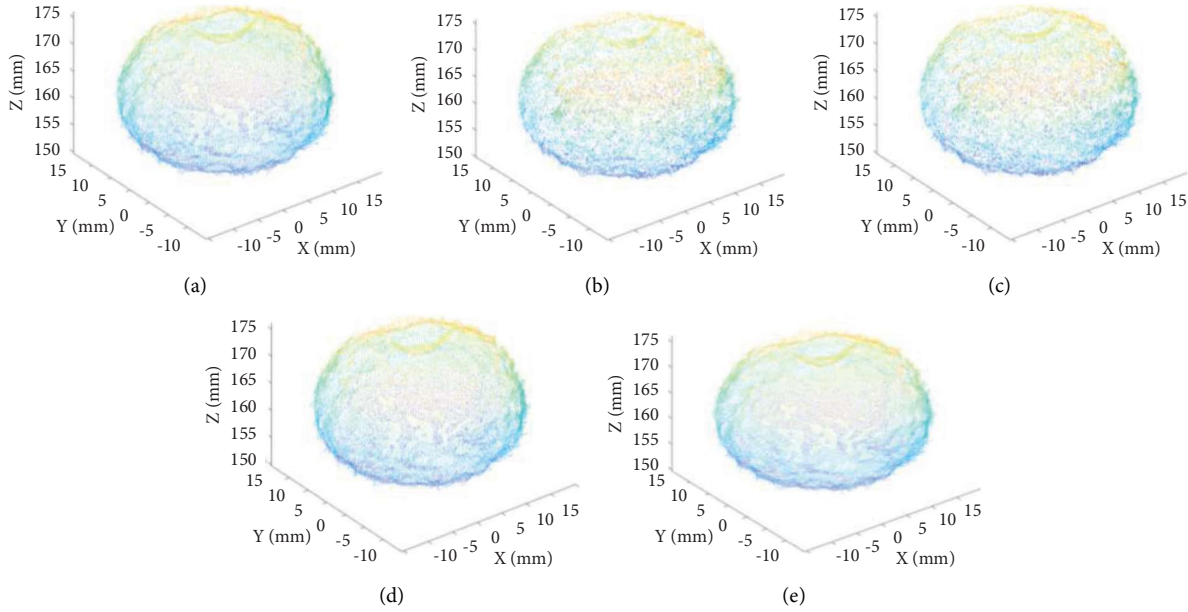


FIGURE 8: Simplification effect of different sampling methods. (a) 3D voxel grid filter; (b) curvature sampling; (c) random sampling; (d) uniform sampling; (e) distance sampling.

reconstructed model volume was calculated by Geomagic Studio. RVE is given by the following equation:

$$\text{RVE} = \frac{V_2 - V_1}{V_1} \times 100\%, \quad (10)$$

where V_1 represents the area of the actual volume and V_2 represents the area of the reconstructed model volume.

As can be seen from Table 2, the NMV and NMF of the Poisson reconstruction and those of the screened Poisson reconstruction algorithm are very close, and the NMV and NMF of the greedy projection triangulation algorithm and those of the Delaunay triangulation algorithm are also similar. From the point of view of the number of model vertices and the number of faces, the reconstruction effects of Poisson reconstruction and screened Poisson reconstruction algorithm were better than other algorithms. From the perspective of the RVE of the model, the screened Poisson reconstruction algorithm has the smallest volume error (1.06%), which showed that its reconstruction accuracy is better than other algorithms. It can be seen from Figure 9 that not only does the reconstruction model reconstructed by the screened Poisson reconstruction algorithm have obvious fruit details but also the model is smooth and complete without redundant facets on the surface. So, the

screened Poisson reconstruction algorithm has the best reconstruction effect. The surface details of the model reconstructed by the greedy projection reconstruction and triangulation reconstruction algorithms are not prominent. So, the reconstruction effect was relatively poor. Therefore, the screened Poisson reconstruction algorithm was considered to be the most suitable algorithm to reconstruct the 3D model of the *Rosa roxburghii* fruit.

3.4. Effects of Octree Depth Value on Reconstruction Results.

In order to obtain a high-precision 3D model, the effect of the Octree depth value on the accuracy of the model reconstructed by the screened Poisson reconstruction algorithm was studied in this section. In the screened Poisson reconstruction algorithm, the function space needed to be discretized, the bounding box of the rectangular parallelepiped containing all the point clouds was subdivided through the Octree, and then the Poisson equation was solved. Generally, the greater the Octree depth value is, the richer the retained details are and the higher the accuracy of the surface reconstruction is. However, the reconstruction time is also affected by the Octree depth value. With the increase of the Octree depth value, the reconstruction time was longer and the efficiency showed a downward trend. In

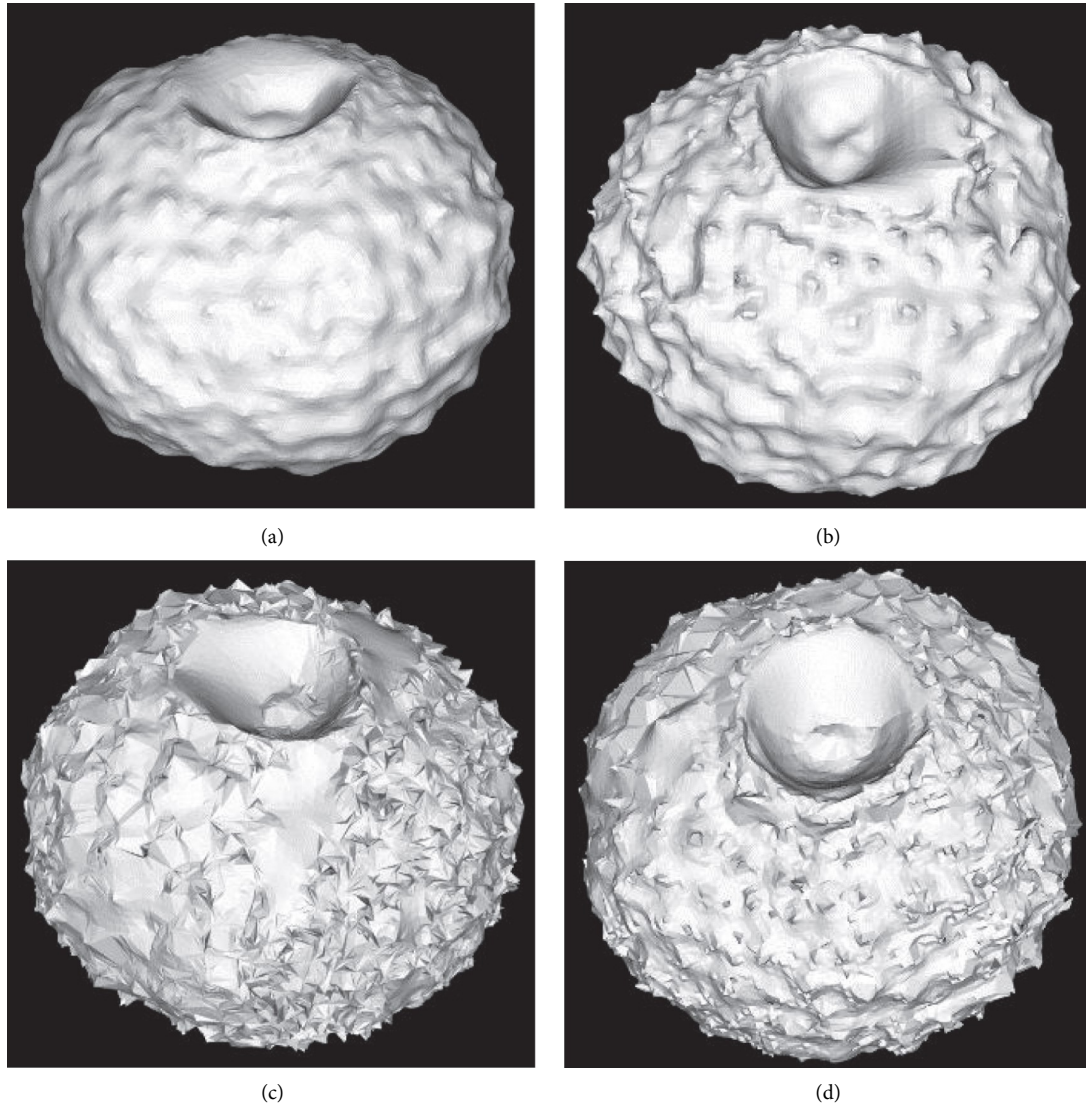


FIGURE 9: Effect of *Rosa roxburghii* fruit reconstruction with different reconstruction algorithms. (a) Poisson reconstruction; (b) screened Poisson reconstruction; (c) greedy projection; (d) Delaunay triangulation.

TABLE 2: Comparison of reconstruction models of different reconstruction algorithms.

Reconstruction algorithm	NMV	NMF	Volume (cm ³)	RVE (%)
Poisson	49350	98692	14.39	1.33
Screened Poisson	51781	101152	14.35	1.06
Greedy projection	22341	41713	14.47	1.90
Delaunay triangulation	23059	42584	14.44	1.69

order to evaluate the accuracy of the 3D reconstruction algorithm of *Rosa roxburghii* fruit in this paper, the REV (equation (10)) was used to evaluate the effect of this reconstruction method. Table 3 shows the relationship between the Octree depth value and the reconstruction effect, reconstruction time, and volume relative error.

As is shown in Table 3, as the Octree depth value increases, the NMV, NMF, and T_{all} increase, and the REV first decreases and then increases. When the Octree depth value is 10, the NMV, NMF, and T_{all} increase, but the REV at this time is still 1.76%. When the Octree depth value is 7, the REV of the reconstruction model is the smallest. Therefore,

TABLE 3: Relationship between the Octree depth value and the volume error.

Octree depth	NMV	NMF	Volume (cm ³)	T (s)	REV (%)
6	12891	25778	14.53	1	2.32
7	51781	101152	14.35	2	1.06
8	115245	230482	14.44	5	1.69
9	330750	661492	14.45	23	1.76
10	1020029	2040052	14.45	96	1.76

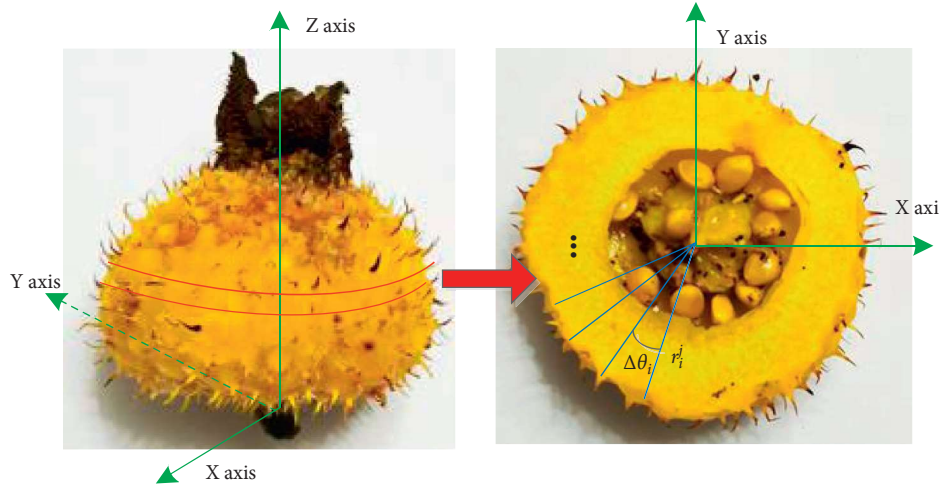


FIGURE 10: Schematic diagram of calculation of sectional area.

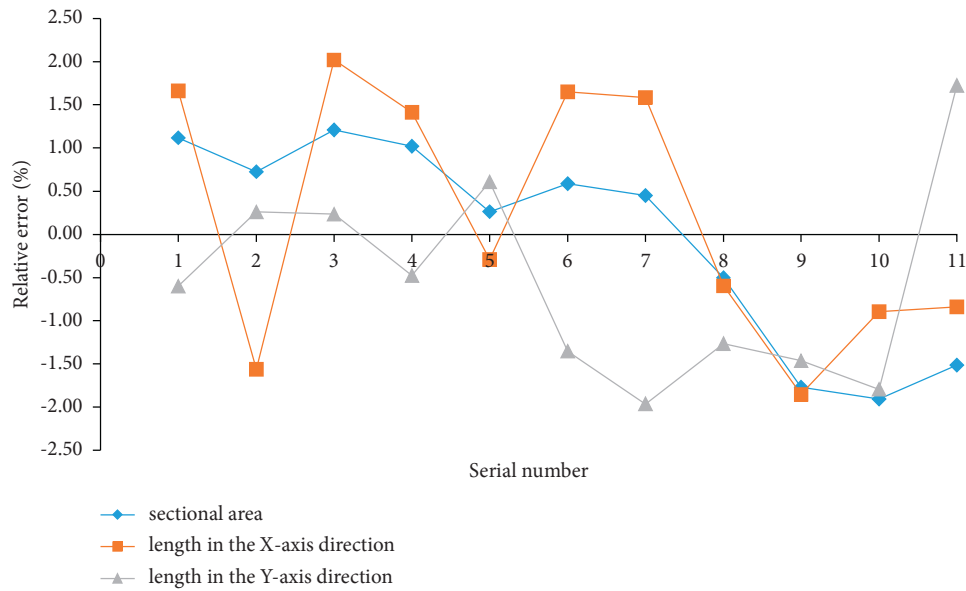


FIGURE 11: Relative error of sectional area and length.

the Octree depth value of the screened Poisson reconstruction algorithm is selected as 7.

3.5. Verification of 3D Reconstruction. In order to verify the consistency between the reconstructed model and the actual fruit shape, the peripheral area, the length in the x -axis direction, and the length in the y -axis direction of the

corresponding section were calculated step by step. Along the z -axis, the *Rosa roxburghii* fruit was sliced with a thickness of 2 mm. In this article, the internal structure of *Rosa roxburghii* fruit was ignored, and only the external shape was verified. The schematic diagram of calculating the peripheral sectional area, the length in the x -axis direction, and the length in the y -axis direction is shown in Figure 10. The sectional area A^j was integrated as follows [46]:

$$A^j = \sum_{i=0}^n \frac{\Delta\theta_i \pi (r_i^j)^2}{360}, \quad (11)$$

where $\Delta\theta_i$ is the stepping angle, r_i^j is the radius of the stepping angle, and n is the number of stepping angles.

The slice peripheral sectional area and length of the reconstructed model were calculated in the 3D modeling software UG. The actual peripheral sectional area and length were manually measured using equation (11). The relative error of sectional area and length between actual measurement and 3D reconstruction model is shown in Figure 11. The mean absolute percentage error is calculated as $\text{MAPE} = (1/n) \sum_0^n |x_m - x_r/x_m|$ (x_m is measured values, x_r is model values). The MAPE of the peripheral sectional area is 1.01%, the MAPE of the length in the x -axis direction is 1.30%, and the MAPE of the length in the y -axis direction is 1.06%. The results illustrated this model can better reconstruct the actual curved surface of *Rosa roxburghii* fruit, and the method provides a reference for the development of the related application.

4. Conclusions

In this paper, a 3D laser scanner was used to acquire point cloud data on the surface of a *Rosa roxburghii* fruit. The segmentation algorithm and the simplification algorithm were implemented to obtain the point cloud data which is conducive to model reconstruction. The Poisson reconstruction algorithm, the screened Poisson reconstruction algorithm, the greedy projection triangulation algorithm, and the Delaunay triangulation algorithm were used to reconstruct the fruit model. In order to verify the accuracy of the reconstruction model, the volume of the reconstructed model obtained using the point cloud was compared with the volume measured manually. The main findings can be summarized as follows:

- (1) A segmentation algorithm combining statistical outlier removal and radius outlier removal is proposed, and the fruit thorns on the *Rosa roxburghii* fruit model can be effectively removed by the segmentation algorithm.
- (2) Compared with the curvature sampling method, random sampling method, uniform sampling method, and distance sampling method, the average error of the reconstruction model using the 3D voxel grid filter method is the smallest, and the detailed features are obviously retained.
- (3) Compared with the greedy projection triangulation algorithm, Delaunay triangulation algorithm, and Poisson reconstruction algorithm, the reconstruction model using the screened Poisson reconstruction algorithm has the most vertices and facets, and no holes are generated. When the Octree depth value is set to 7, the REV of the reconstruction model is the smallest.

- (4) The MAPE of the peripheral sectional area is 1.01%, which shows that this model can better reconstruct the actual curved surface of the *Rosa roxburghii* fruit.

Data Availability

The data used to support the findings of this study are available from the corresponding author upon request.

Conflicts of Interest

The authors declare that they have no conflicts of interest.

Acknowledgments

This work was supported by the Natural Science Foundation of Guizhou (Grant no. [2019]1233), the Major Science and Technology Projects of Guizhou (Grant no. [2019]3003), and the Special Fund of Chinese Central Government Guidance for Local Science and Technology Development (Grant no. [2016]4006).

References

- [1] J. Yan, Y. Zhao, L. Zhang et al., "Recognition of rosa roxburghii in natural environment based on improved faster RCNN," *Transactions of the Chinese Society of Agricultural Engineering*, vol. 35, no. 18, pp. 143–150, 2019.
- [2] Q. Yang, D. Zhang, A. K. Farha et al., "Phytochemicals, essential oils, and bioactivities of an underutilized wild fruit cili (*Rosa roxburghii*)," *Industrial Crops and Products*, vol. 143, Article ID 111928, 2020.
- [3] J. Xu, S. K. Vidyarthi, W. Bai, and Z. Pan, "Nutritional constituents, health benefits and processing of rosa roxburghii: a review," *Journal of Functional Foods*, vol. 60, Article ID 103456, 2019.
- [4] C. Liu, L.-P. Chan, and C.-H. Liang, "The anti-aging activities against oxidative damages of *Rosa roxburghii* and multi-fruit concentrate drink," *Journal of Food and Nutrition Research*, vol. 7, no. 12, pp. 845–850, 2020.
- [5] G. Liu, Y. Si, and J. Feng, "3D reconstruction of agriculture and forestry crops," *Transactions of the Chinese Society for Agricultural Machinery*, vol. 45, no. 6, pp. 38–46, 2014.
- [6] C. Zhao, S. Lu, X. Guo, J. Du, W. Wen, and T. Wen, "Advances in research of digital plant: 3D digitization of plant morphological structure," *Scientia Agricultura Sinica*, vol. 48, no. 17, pp. 3415–3428, 2015.
- [7] Y. Wang, W. Wen, X. Guo, C. Zhao, and N. University, "Three-dimensional reconstruction of plant leaf blade based on point cloud data," *Journal of Agricultural Science and Technology A*, vol. 16, no. 5, pp. 83–89, 2014.
- [8] S. Li, Y. Zhu, H. Liu et al., "Research and realization of wheat leaf three-dimensional visualization based on NURBS surface," *Journal of Agricultural Science and Technology A*, vol. 18, no. 3, pp. 89–95, 2016.
- [9] F. Zhu, S. Thapa, T. Gao, Y. Ge, H. Walia, and H. Yu, "3D reconstruction of plant leaves for high-throughput phenotyping," in *Proceedings of the 2018 IEEE International Conference on Big Data (Big Data)*, Seattle, WA, USA, December 2019.

- [10] K. Yin, H. Huang, P. Long, A. Gaissinski, M. Gong, and A. Sharf, "Full 3D plant reconstruction via intrusive acquisition," *Computer Graphics Forum*, vol. 35, no. 1, pp. 272–284, 2016.
- [11] L. Quan, P. Tan, G. Zeng, L. Yuan, J. Wang, and S. B. Kang, "Image-based plant modeling," *ACM Transactions on Graphics*, vol. 25, no. 3, pp. 599–604, 2006.
- [12] C. Wang, X. Guo, S. Wu, B. Xiao, and J. Du, "Three dimensional reconstruction of maize ear based on computer vision," *Transactions of the Chinese Society for Agricultural Machinery*, vol. 45, no. 9, pp. 274–279, 2014.
- [13] J. Yousfi, S. Lahouar, and A. B. Amara, "Study on the strategy of 3D images based reconstruction using a camera attached to a robot arm," *Engineering Research Express*, vol. 2, no. 2, Article ID 025006, 2020.
- [14] D. M. Kempthorne, I. W. Turner, J. A. Belward et al., "Surface reconstruction of wheat leaf morphology from three-dimensional scanned data," *Functional Plant Biology*, vol. 42, no. 5, pp. 444–451, 2015.
- [15] C. Hu, P. P. Li, P. Li, and Z. Pan, "Phenotyping of poplar seedling leaves based on a 3D visualization method," *International Journal of Agricultural and Biological Engineering*, vol. 11, no. 6, pp. 145–151, 2018.
- [16] H. A. Tinoco, D. A. Ocampo, F. M. Peña, and J. R. Sanz-Urbe, "Finite element modal analysis of the fruit-peduncle of *Coffea arabica* L. var. Colombia estimating its geometrical and mechanical properties," *Computers and Electronics in Agriculture*, vol. 108, pp. 17–27, 2014.
- [17] G. X. Sun and X. C. Wang, "Three-dimensional point cloud reconstruction and morphology measurement method for greenhouse plants based on the kinect sensor self-calibration," *Agronomy-Basel*, vol. 9, no. 10, Article ID 9100596, 2019.
- [18] D. Xie, X. Wang, J. Qi et al., "Reconstruction of single tree with leaves based on terrestrial LiDAR point cloud data," *Remote Sensing*, vol. 10, no. 5, p. 18, 2018.
- [19] D. Zermas, V. Morellas, D. Mulla, and N. Papanikolopoulos, "3D model processing for high throughput phenotype extraction—the case of corn," *Computers and Electronics in Agriculture*, vol. 172, Article ID 105047, 2020.
- [20] Z. Liu, X. Xiao, S. Zhong et al., "A feature-preserving framework for point cloud denoising," *Computer-Aided Design*, vol. 127, Article ID 102857, 2020.
- [21] W. Zhang, G. Liu, C. Guo, Z. Zong, and X. Zhang, "Apple tree leaf three-dimensional reconstruction based on point cloud," *Transactions of the Chinese Society for Agricultural Machinery*, vol. 48, no. S1, pp. 103–109, 2017.
- [22] P. J. Besl and N. D. McKay, "A method for registration of 3-D shapes," *IEEE Transactions on Pattern Analysis and Machine Intelligence*, vol. 14, no. 2, pp. 239–256, 1992.
- [23] M. J. Rakotosaona, V. La Barbera, P. Guerrero, N. J. Mitra, and M. Ovsjanikov, "PointCleanNet: learning to denoise and remove outliers from dense point clouds," *Computer Graphics Forum*, vol. 39, no. 1, pp. 185–203, 2019.
- [24] X. Ren, W. Wang, and X. Shijun, "An innovative segmentation method with multi-feature fusion for 3D point cloud," *Journal of Intelligent and Fuzzy Systems*, vol. 38, no. 1, pp. 345–353, 2019.
- [25] X. Shi, T. Liu, and X. Han, "Improved iterative closest point (ICP) 3D point cloud registration algorithm based on point cloud filtering and adaptive fireworks for coarse registration," *International Journal of Remote Sensing*, vol. 41, no. 8, pp. 3197–3220, 2020.
- [26] T. Dziubich, J. Szymański, A. Brzeski, J. Cychnerski, and W. Korlúb, "Depth images filtering in distributed streaming," *Polish Maritime Research*, vol. 23, no. 2, pp. 91–98, 2016.
- [27] F. Bernardini, J. Mittleman, H. Rushmeier, C. Silva, and G. Taubin, "The ball-pivoting algorithm for surface reconstruction," *IEEE Transactions on Visualization and Computer Graphics*, vol. 5, no. 4, pp. 349–359, 1999.
- [28] M. Kazhdan, M. Bolitho, and H. Hoppe, "Poisson surface reconstruction," in *Proceedings of the Eurographics Symposium On Geometry Processing*, Cagliari, Sardinia, June 2006.
- [29] M. Kazhdan and H. Hoppe, "Screened poisson surface reconstruction," *ACM Transactions on Graphics*, vol. 32, no. 3, pp. 1–13, 2013.
- [30] G. Guennebaud and M. Gross, "Algebraic point set surfaces," *ACM Transactions on Graphics*, vol. 26, no. 3, p. 23, 2007.
- [31] H. Edelsbrunner and E. P. Mücke, "Three-dimensional alpha shapes," *ACM Transactions on Graphics*, vol. 13, no. 1, pp. 43–72, 1994.
- [32] J. Liu, D. Bai, and L. Chen, "3-D point cloud registration algorithm based on greedy projection triangulation," *Applied Sciences*, vol. 8, no. 10, p. 1776, 2018.
- [33] P. J. Green and R. Sibson, "Computing dirichlet tessellations in the plane," *The Computer Journal*, vol. 21, no. 2, pp. 168–173, 1978.
- [34] D. Sun, H. Guo, Y. Li, and N. Lekui, "Method of rigid registration based on poisson reconstruction of local sample points," *Journal of Mechanical Engineering*, vol. 54, no. 15, pp. 141–149, 2018.
- [35] A. Maiti and D. Chakravarty, "Performance analysis of different surface reconstruction algorithms for 3D reconstruction of outdoor objects from their digital images," *SpringerPlus*, vol. 5, p. 26, 2016.
- [36] A. Bowyer, "Computing dirichlet tessellations," *The Computer Journal*, vol. 24, no. 2, pp. 162–166, 1981.
- [37] E. S. Coakley and V. Rokhlin, "A fast divide-and-conquer algorithm for computing the spectra of real symmetric tri-diagonal matrices," *Applied and Computational Harmonic Analysis*, vol. 34, no. 3, pp. 379–414, 2013.
- [38] S. Methirumangalath, A. D. Parakkat, S. S. Kannan, and R. Muthuganapathy, "Reconstruction using a simple triangle removal approach," in *Proceedings of the SIGGRAPH Asia 2017 Technical Briefs*, p. 27, Bangkok, Thailand, November 2017.
- [39] B. Zou, H. Qiu, and Y. Lu, "Point cloud reduction and denoising based on optimized downsampling and bilateral filtering," *IEEE Access*, vol. 8, Article ID 159479, 2020.
- [40] Y. Li, H. Liu, Y. Tao, and J. Liao, "Reasoning mechanism: an effective data reduction algorithm for on-line point cloud selective sampling of sculptured surfaces," *Computer-Aided Design*, vol. 113, pp. 48–61, 2019.
- [41] Q. Shao, T. Xu, and T. Yoshino, "Point cloud simplification algorithm based on particle swarm optimization for online measurement of stored bulk grain," *International Journal of Agricultural and Biological Engineering*, vol. 9, no. 1, pp. 71–78, 2016.
- [42] Z. N. Sultani and R. F. Ghani, "Kinect 3D point cloud live video streaming," *Procedia Computer Science*, vol. 65, pp. 125–132, 2015.
- [43] X.-F. Han, J. S. Jin, M.-J. Wang, W. Jiang, L. Gao, and L. Xiao, "A review of algorithms for filtering the 3D point cloud," *Signal Processing: Image Communication*, vol. 57, pp. 103–112, 2017.

- [44] Z. Ma, "A point cloud simplification algorithm based on kd-tree and curvature samplin," *Science Surveying and Mapping*, vol. 35, no. 6, pp. 67–69, 2010.
- [45] B.-Q. Shi, J. Liang, and Q. Liu, "Adaptive simplification of point cloud using -means clustering," *Computer-Aided Design*, vol. 43, no. 8, pp. 910–922, 2011.
- [46] Z. Cai, C. Jin, J. Xu, and T. Yang, "Measurement of potato volume with laser triangulation and three-dimensional reconstruction," *IEEE Access*, vol. 8, pp. 176565–176574, 2020.